Ultrastructural Evidence of Dermal Gadolinium Deposits in a Patient with Nephrogenic Systemic Fibrosis and End-Stage Renal Disease

Josef A. Schroeder[*], Christian Weingart[†], Brigitte Coras[‡], Ingrid Hausser[§], Stephan Reinhold[†], Matthias Mack[†], Volker Seybold[ll], Thomas Vogt[‡], Bernhard Banas[†], Ferdinand Hofstaedter[*], Bernhard K. Krämer[†**]

*Departments of *. Pathology, †. Nephrology, and ‡. Dermatology, Regensburg University Hospital, Regensburg, Germany; §. Department of Dermatology, Heidelberg University Hospital, Heidelberg, Germany; ll. Application Development Transmission Electron Microscopy, Carl Zeiss Nano Technology Systems GmbH, Oberkochen, Germany; and **. Medizinische Klinik I, Marienhospital Herne, Ruhr University, Bochum, Germany*

Correspondence: Dr. Christian Weingart, Klinik und Poliklinik für Innere, Medizin II–Nephrologie, University of Regensburg, Franz-Josef-Strauβ-Allee 11, 93053 Regensburg, Germany. Phone: +49-941-944-0; Fax: +49-941-944-7302; E-mail: christian.weingart@klinik.uni-regensburg.de

Abstract

Background and objectives: The pathogenesis of acquired nephrogenic systemic fibrosis recently described for patients with renal insufficiency and a history of exposition to gadolinium-based magnetic resonance contrast agents is not completely understood. A role for circulating fibroblasts in the fibrosing tissue is hypothetical, and the mechanism of the assumed trigger function of gadolinium remains elusive.

Design, setting, participants, & measurements: A skin lesion on a 76-yr-old man with symptoms of nephrogenic systemic fibrosis lasting 5 mo was studied at the ultrastructural level. After confirmation of he diagnosis by histopathologic methods, the presence and distribution of gadolinium, iron, calcium, and magnesium by energy filtering transmission electron microscopy was also examined.

Results: The performed electron spectroscopic imaging and electron energy loss spectroscopic analyses on deparaffinized samples revealed deposition of gadolinium in irregular small aggregates that adhered to cell profiles and collagen fibers of the connective tissue, forming a perivascular "gadolinium-deposit zone" in the skin. Traces of iron signal were demonstrated in singular gadolinium-positive deposits, and iron

presence was found in adjacent connective tissue. The ultrastructural cell analysis of the lesion showed among numerous poorly differentiated fibrocytes also higher differentiated cells with myofibroblastic characteristics, including bundles of intermediate filaments and attachment plaques in the cell periphery, indicating an ability of lesional fibroblasts to differentiate into myofibroblastic cells.

Conclusions: These findings support the pivotal role of gadolinium chelates in the development of nephrogenic systemic fibrosis.

The enigma of the recently emerged disease entity now termed "nephrogenic systemic fibrosis" (NSF) becomes a growing challenge relevant to nephrologists, radiologists, and dermatology practitioners. More than 105 references cited ([1]) by the International Center for Nephrogenic Fibrosing Dermopathy Research enclose mostly case reports and patient series since the first clinical and pathologic description has been published in 2000 ([2,3]). Initially referred to as cutaneous disorder present almost exclusively in patients with ESRD, growing clinical and autopsy data now suggest a systemic fibrogenic process that involves many other tissues and various internal organs, such as muscle, myocardium, testes, lungs, and dura ([4]–[13]). The estimation of the prevalence of this painful and tremendously disabling disease seems to be inaccurate because of underdiagnosis and underreporting ([14,15]). Currently, the diagnosis is confirmed by a deep dermal biopsy from affected skin areas showing fibrosis and specific histopathologic features such as identification of $CD34^+$ spindle cells as bone marrow–derived fibrocytes ([3,16]–[18]).

NSF is observed exclusively in patients with renal insufficiency and in most cases with a history of exposition to gadolinium (Gd)-based magnetic resonance (MR) contrast agents ([16,19]–[21]). Gd, introduced in 1988 as a paramagnetic contrast agent, is widely used in MR imaging as a relatively safe complex with an anorganic ligand (linear or macrocyclic chelate) ([22,23]). The stability of the Gd chelate depends on the chemical structure of the chelate itself (cyclic versus linear) but also on the chemical environment (e.g., acidic conditions). Chelates distribute equally in the extracellular compartment and are excreted almost exclusively by the kidney; therefore, their half-life time increases dramatically when kidney function deteriorates. In healthy humans, half-life of Gd chelates is approximately 1.3 h, whereas in patients with ESRD, it is prolonged to approximately 120 h ([22,24]). It has been suggested that the prolonged presence of Gd chelates in the body allows significant release of free Gd^{3+} ions or transmetallation reactions with other competing ions, such as iron, calcium, or magnesium. Finally, free Gd^{3+} ions have been shown to be extremely toxic ([25]–[30]); however, the exact pathogenesis of NSF is still elusive, and the contribution of various risk factors that promote the disease is discussed controversially ([14,24]).

Recently, the presence of Gd in cutaneous biopsies of patients with NSF was demonstrated by two groups that applied scanning electron microscopy/energy-dispersive x-ray (18,31–33) and inductively coupled plasma mass spectroscopy (34). The element visualization in tissue paraffin sections was done by backscattered electrons. The energy filtered transmission electron microscopy (EFTEM) for the analysis of ultrathin resin tissue sections provides a much higher structural resolution (0.1 nm) (35) and sensitivity (36–41) for element detection and localization. The EFTEM technique is based on the phenomenon that primary beam electrons that pass through a sample interact with target atoms of the specimen and lose a defined, element-specific amount of energy ("inelastic scattering"). The energy loss of the beam electrons is analyzed by an in-column integrated energy filter (spectrometer), and a special aperture selects electrons at the element-specific energy-loss level for imaging the elemental distribution in the sample.

In biologic specimens, two modes of EFTEM are widely used: Electron energy-loss spectroscopy (EELS) records the whole energy-loss range (0 to 2500 eV) as a complete energy spectrum, where "edges" at characteristic energy levels provide information about the chemical composition of the sample. The spatial distribution of elements present in the sample can be mapped by electron spectroscopic imaging (ESI) using inelastically scattered electrons with the element-specific energy loss (42–50).

Materials and Methods

For light histopathology, a skin-punch biopsy taken from an obviously affected area of the thigh was fixed in 4% buffered formalin (pH 7.0), paraffin-embedded, and routinely stained for hematoxylin and eosin, as well as CD34 and CD68 for immunohistochemical evaluation. For the ultrastructure study, guided (by the hematoxylin and eosin and CD34^{+} sections) tissue cores were punched from the wax skin block (2 mm diameter), deparaffinized in xylene, rehydrated with ethanol and cacodylate buffer, and postfixed with 4% glutaraldehyde in 0.1 M cacodylate buffer (pH 7.3) and subsequently with aqueous 1% osmium tetroxide (both 1 h). This tissue was routinely dehydrated in an automated manner in graded ethanols (LYNX; Leica, Vienna, Austria) and embedded in epoxy resin (EMbed 812; all reagents Science Services, Munich, Germany). Double toluidine blue/basic fuchsin-stained semithin sections (0.8 μm) were used for target structure block trimming for the ultramicrotomy (Ultracut S; Leica). For conventional EM, examination, and live telepathology consultation via the Internet with a remote expert, the produced ultrathin sections (80 nm) were double stained with aqueous uranyl acetate and lead citrate and examined in the LEO912AB (Carl Zeiss, Oberkochen, Germany) EFTEM, operated at 80 kV in the zero-loss mode. In this mode (routine EM setting for

diagnostic tissue examination), inelastically scattered electrons (i.e., chromatic aberration) are filtered out, leading to crisp images with enhanced contrast, which were digitally acquired by a 1×1-k pixel side-entry fast frame–transfer CCD camera equipped with a fiber optic coupled YAG scintillator (TRS, Moorenweis, Germany).

To get a second opinion for the diagnostic evaluation of the ultrastructural findings, we used our telemicroscopy system designed in a server client architecture ([51]). An external expert (in this case, the ultrastructural skin pathology expert I.H. from the University of Heidelberg) as a client could remotely operate our EM via the Internet from her office and perform a direct examination of the section instead of interpreting preselected images.

Elemental microanalysis was performed on very thin sections (approximately 40 nm) to minimize multiple electron scattering in the sample (35°-angle diamond knife; Diatome, Biel, Switzerland) collected on foil-uncoated copper grids (300 Mesh, hexagonal bar) without any heavy metal poststaining. For avoidance of thermal drift during tissue examination, ultrathin sections were stabilized in the EM for some minutes under bright electron-beam illumination conditions at low magnification. The EFTEM was operated at 100 kV with a tungsten cathode; the in-column energy spectrometer was operated at 20-eV slit width and calibrated for spectroscopic imaging with inelastically scattered electrons (ESI). Specific EELS of small specimen regions in the specimen (suspect deposits) were acquired in spot mode of the parallel EELS method at a 25,000 magnification setting. We used the EFTEM software package iTEM (version 5; OSIS, Muenster, Germany) for the digital ESI imaging and EELS spectra acquisition and evaluation. For net elemental mapping of Gd, calcium, and magnesium, the "tree-window" method and the power law background calculation ([37]) were applied. For this purpose, images were obtained at different energy losses ΔE: One window at the element specific most probable energy loss (e.g., $Gd_{M4, 5} = 1193$ eV) and two windows for background evaluation (W1 = 1164 eV, W2 = 1140 eV) ([52]). An additional ultrastructural image was acquired in front of the carbon ionization edge (250 eV; high-contrast imaging [HCI]), which was inverted and used for the electronically superimposed net mapping of the element.

The Case: Clinical Data

A 76-year-old man presented in our vascular surgery department in September 2006 as a result of peripheral artery disease, which had led to an ulcerous lesion underneath his left great toe. His medical history at that time included arterial hypertension, diabetes present for several years, coronary artery disease, and stenosis of both carotid arteries. Surgical revascularization of the coronary artery had already been undertaken approximately 4 yr before as well as surgical

desobliteration of the carotid arteries. Renal function at presentation in September 2006 was already reduced to a GFR of 18 ml/min. Awareness of impaired renal function contributed to the decision to perform MR tomography scans to avoid renal toxicity of conventional iodinated contrast agents. Within 2 weeks, the patient underwent three MR tomography scans in total, two of which were MR angiographies, receiving in total 49.5 mmol of gadopentetate. After femoropedal bypass surgery, hemodialysis had to be started because of progressive renal failure 2 d after surgery. Laboratory values at that time were as follows: Serum sodium 140 mmol/L, serum potassium 4.7 mmol/L, serum calcium 2.05 mmol/L, serum phosphorus 0.75 mmol/L, whole-blood standard bicarbonate 21.8 mmol/L, C-reactive protein 50.0 mg/dl, serum albumin 34.3 g/L, parathormone 134 ng/L, transferrin saturation 24%, hematocrit 29.5%, white blood cell count 9.21/nl, and platelets 227/nl. Daily medication consisted of bisoprolol (2.5 mg), calcium carbonate (500 mg), oral iron (100 mg), folic acid (5 mg), amlodipine (5 mg), doxazosine (4 mg), and ranitidine (300 mg); darbepoietin α (10 μg) once weekly; and subcutaneous insulin according to blood glucose levels. Hemodialysis was initially performed by using a Demers jugular dialysis catheter for 2 mo until a newly created cimino fistula could be used. In February 2007, 4 mo after initiation of hemodialysis, the patient complained of worsening mobility of his lower extremities. Furthermore, the femoral skin had increasingly thickened during the weeks before, which contributed to a significant decrease of mobility. For confirmation of the suspected diagnosis of NSF, a deep punch biopsy of the skin of the medial right thigh was performed. For ruling out differential diagnoses such as autoimmune disorders such as scleroderma and pseudosclerodermia caused by paraproteinemia, laboratory tests for ANA, ANCA, single strand annealing A, single strand annealing B, ribonucleoprotein protein particles, Sm, and topoisomerase I antibodies as well as protein electrophoresis were performed and tested negative.

Histopathology

Representative histologic changes of the skin and the subcutaneous tissue are shown in Figure 1. Whereas the epidermis showed no noticeable changes, the corium and the subcutis showed pronounced fibrosis with only discrete perivascular inflammatory infiltrates. Immunohistochemistry staining for CD34 identified multiple positive spindle-shaped cells as fibrocytes, whereas scattered histiocytes were CD68^{+}, confirming the diagnosis of NSF.

Conventional EM

In the semithin sections of the resin-reembedded skin samples, some blood vessel profiles in proximity to a fat pad of the deep dermis were identified by light microscopy; sweat gland profiles or hair follicles were not found. For EM, the paraffin-embedded material was reprocessed. Apart from the extraction artifacts related to the processing method, the deparaffinized material still allowed the

recognition of cellular membranous structures, desmosomes, cytoskeleton filaments, and inclusions/deposits. The electron microscopic examination of the routinely heavy metal–stained ultrathin sections revealed a dermis with abundant tortuous collagen bundles and elastic fibers, numerous spindle-shaped and elongated fibrocytes, scattered histiocytic cells, and a minimal, mostly perivascular inflammatory infiltrate; all structures exhibited a compromised ultrastructure preservation adequate for deparaffinized tissue (Figure 2). In the peripheral cytoplasm of some of the elongated cells with a cigar-shaped nucleus, bundles of parallel intermediate filaments (5 to 8 nm in thickness) and numerous subplasmalemmal attachment plaques were observed (Figure 2B), indicating myofibroblastic differentiation. A diligent examination of the blood vessel wall revealed tiny, not very electron-dense, material spots at the outer site of the basal lamina and irregularly disseminated in the adjacent connective tissue. These pleomorphic spots showed a fine granular texture and had a size range between 100 and 400 nm; several reached approximately 1000 nm in diameter. We consulted this observation online with a skin ultrastructural pathology expert (I.H.) using our telepathology system, and the retrieved second opinion was consistent with anorganic material deposits such as calcium and/or magnesium, but the question of whether they also contain Gd remained open (Figure 2, C and D).

Electron Spectroscopic Imaging

EFTEM microanalysis was performed on the unstained 40-nm ultrathin sections; and to get an overview of topologic information, the structure contrast was enhanced using only inelastically scattered electrons with an energy loss of $\Delta E = 250$ eV (HCI). The resulting inelastic dark-field images displayed the dermal structures and facilitated the search for the deposits in question (Figure 3C). After selection of adequate specimen areas, the ESI image series for detection of Gd, iron, calcium, and magnesium were acquired and the net element image was calculated, respectively (Figure 3). A superimposition of the net Gd image on the corresponding electronically inverted HCI image shows the element mapping in the specimen: The Gd signal was visible mainly perivascular as deposits multifocally associated with the outer site of the blood vessel basal lamina, profiles of cell bodies and processes, and collagen fibers (Figure 4A). Some electron-dense deposits or inclusions only partially contained Gd; in some areas, the Gd seemed to be localized intracytoplasmatically (Figure 4B). A characteristic parallel EELS spectrum obtained from a Gd-containing perivascular deposit presenting the typical $Gd_{M4, 5}$ "white line" shape is shown in Figure 4C. In a subsequently performed iron elemental mapping at the iron ionization L edge ($Fe_{L2, 3} = 708$ eV), traces of iron signal were demonstrated in singular Gd-positive deposits and in very small inclusions (measured range of 40 to 150 μm) in the adjacent connective tissue (Figure 4D). The respective parallel EELS

spectra revealed a weak iron signal peak (data not shown). Calcium and magnesium were not detected.

Discussion

These data strongly suggest a relationship between exposition to Gd and development of NSF in patients with severe renal insufficiency. First reports of Gd deposits within skin specimens of patients with confirmed NSF were published in 2007 ([18,31](#)–[34](#)), supporting a causal relationship between Gd exposition and NSF; however, there may be triggers of the disorder other than Gd indicating that pathogenesis of NSF requires a pattern of premises that facilitate and promote fibrosis ([53](#)).

Diagnosis is still based on the detection of histopathologic signs of fibrosis in combination with significant amounts of CD34^{+} fibrocytes ([3](#)), which is suggestive but not exclusively specific for NSF. For ruling out differential diagnoses such as scleroderma or paraprotein-associated scleromyxedema, further laboratory tests have to be performed. In our patient, among numerous poorly differentiated fibrocytes, we also found a few higher differentiated ones, which phenotypically resembled myofibroblastic cells presenting classical bundles of intermediate filaments and attachment plaques in the peripheral cytoplasm ([54](#)). This finding is in line with the currently discussed etiopathogenic role of free circulating fibrocytes in NSF, which are able to differentiate into contractile myofibroblasts that appear also in many fibrotic lesions ([14,55,56](#)). A high amount of myofibroblasts in progressing NSF skin lesions was also reported by Swartz et al. ([4](#)), who found similarities to wound-healing processes. Although the finding of myofibroblasts was not surprising, we also detected tiny deposits, primarily noticed only at the external basal lamina aspect of the blood vessels. These deposits were rated as anorganic deposits that could contain Gd, which could be confirmed by applying the EELS and ESI imaging technology. These small Gd accumulations were present in large numbers disseminated perivascular in a zone of approximately 5-μm width. In greater distance from the blood vessels, only singular, rarely dispersed deposits between collagen bundles were found. Some Gd signal–positive deposits showed the coexistence with scanty iron-positive signals and iron traces in the adjacent connective tissue. This finding substantiates previous detection of iron deposits ([32,33](#)). A contamination of our samples by an iron-containing microtome blade could be excluded using a diamond knife and avoiding any contact of our samples with iron-containing surfaces. The quantitative data of other authors ([18,31](#)–[34](#)) revealed intralesional Gd amounts in the 5- to 106-ppm range. Actually, these deposits still persisted 3 yrs after the last Gd administration. Our ESI images displayed that Gd is distributed in small, irregular deposits or aggregates of 100 to 1000 nm arranged in a perivascular zone of approximately 5-μm width. Showing such a distinct perivascular distribution of Gd with a high resolution allowing discrimination of even small-sized particles, our observations

refine and extend the previous reports detecting Gd deposits in the skin by other, lower resolving methods (18,31–33) and give us a better spatial illustration of the Gd distribution in the skin lesions. The co-localization of Gd and iron signals in the same deposits advocates the transmetallation hypothesis of Gd chelates, which is probably one important trigger or at least a co-factor of the disease (14,20–23,57). To our knowledge, this is the first study to demonstrate Gd deposits at high EM resolution and sensitivity of the EELS technique. The EFTEM technology is an established method and has been applied in a number of life science studies (36,38,42), generating substantial information concerning the nonpinocytotic interaction of exogenous particles with cells (44,45) or elucidating the role of different elements in pathologic lesions (46–50).

Probably because of the reprocessing, we were not able to show signs of cytotoxicity caused by Gd as described by Mizgerd et al. (30) on dermal cells and macrophages in vitro. In addition, they reported Gd located in lysosomes and nuclei as well as signs of apoptosis. In our material, we could not find any intranuclear Gd signal. Although we were able to detect a predominantly perivascular element dispersion, we could not obtain any information about possible vasculopathic signs or possible blood vessel wall leakage reported by Mendoza et al. (10).
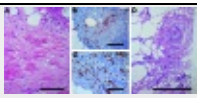
Examinations of future samples should provide more insight into the interaction of Gd with the affected tissue. For addressing this question, particular potential will be offered by the analysis of the near-edge fine structure of the EELS spectra (ELNES method) (58,59), which may provide insight into the chemical bonding characteristics between Gd and other elements or compounds in situ (e.g., in cryosections of hydrated tissue [36,41]).

Conclusions

The ultrastructural examination and EFTEM element analysis of skin lesions of a patient with ESRD and histopathologically confirmed NSF revealed data displaying a mainly perivascular-dispersed Gd deposition. In addition, co-localization of iron could be confirmed. The infiltrating fibrocytes show distinct signs of myofibroblastic differentiation. Our results clarify that Gd and possibly iron may play a pivotal role in the development of fibrotic disorders such as NSF, although we could not provide any functional data. Further investigations on the pathogenesis of NSF may require ultrastructural analyses such as the EFTEM technique as well as in vivo and in vitro models.
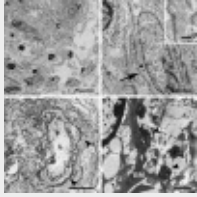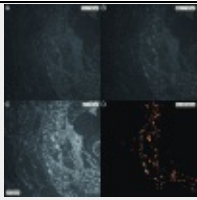
Disclosures

None.

Figure 1. Deep skin biopsy. (A) Hematoxylin and eosin stain showing dense dermal fibrosis with spindle cells and slight perivascular cellular infiltrate. (B) CD34$^+$ spindle cells between collagen bands. (C) Area with numerous CD68$^+$ histiocytic cells. (D) Double toluidine blue/fuchsin-stained semithin resin section showing a fragment of the wax-reprocessed tissue containing a blood vessel selected for EM study. Bar = 100 µm.
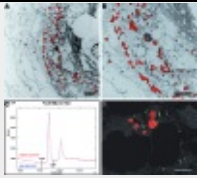
Figure 2. Conventional EM of deparaffinized skin tissue. (A) Low-magnification overview of the dermis displaying bundles of collagen (C) with clefts, profile of a small blood vessel (V), histiocytes (H), fibroblastic (F), and inflammatory cells. Bar = 10 µm. (B) Closer view at a higher differentiated elongated cell presenting myofibroblastic hallmarks including attachment plaques (arrow) and bundles of intermediate filaments (* and insert). Bar = 2 µm (insert bar = 500 nm). (C) Overview showing a blood vessel with empty lumen (L) and numerous tiny deposits (arrowheads) at the external side of the basal lamina. Bar = 10 µm. (D) Features noted at higher magnification of the irregular-shaped deposits with fine-granular texture mostly adhering to the basal membrane (BM). Bar = 500 nm. (C and D) Images captured during telepathologic second-opinion retrieval.

Figure 3. ESI: Overview of images taken from an unstained skin section showing the perivascular region of a blood vessel using inelastic scattered electrons. (A) Background image at 1164 eV energy loss. (B) Image taken at the maximum of the Gd-specific signal at 1193 eV energy loss. (C) Structure-sensitive image (HCI) taken at 250 eV energy loss before the carbon-specific signal; note the dark field–like structure visualization. (D) Net Gd signal calculated by subtracting the extrapolated background image from the Gd-specific signal. The obtained image reflects the Gd distribution and is displayed in red color; yellow color is attributed to more intense element signal. Magnification, ×2100.

Figure 4. ESI and parallel EELS. (A) Gd mapping in the skin lesion at low magnification. The net Gd signal image is superimposed on the inverted HCI image showing the precise localization of the signals as red spots on the tissue structures. Note the dispersed Gd aggregates in the perivascular zone of the blood vessel and only singular deposits in the adjacent tissue. (B) Higher magnification of portion of A showing detailed features of the Gd deposits and their multifocal association with the blood vessel basal lamina, cell profiles, and collagen fibrils. In the dark lysosomal structure, Gd signal is visible only at the periphery. (C) Parallel EELS spectrum. The confirmation of a particular element is demonstrated by its defined energy-loss edge at the energy level necessary for atom inner shell ionization. Record of the measured (spot mode) Gd signal (red) displaying the typical "white line" peaks characteristic for Gd. For comparison, the reference Gd spectrum from the element atlas (blue). (D) Simultaneous Gd and iron mapping in deep dermis. Both net Gd (red) and iron (green) signal were combined with the original HCI image. Note the iron signal co-localization in the Gd deposits (orange dots) and their periphery as well as small iron aggregates in the adjacent tissue. Bar = 2 µm (all images).

Acknowledgments

References

1. Cowper SE: Nephrogenic Fibrosing Dermopathy [NFD/NSF Website]. 2001–2007. Available at: http://icnfdr.org. Accessed November 5, 2007

2. Cowper SE, Robin HS, Steinberg SM, Su LD, Gupta S, LeBoit PE: Scleromyxoedema-like cutaneous diseases in renal-dialysis patients. Lancet. 356:: p. 1000 –1001, 2000. [PubMed]

3. Cowper SE, Su LD, Bhawan J, Robin HS, LeBoit PE: Nephrogenic fibrosing dermopathy. Am J Dermatopathol. 23:: p. 383 – 393, 2001. [PubMed]

4. Swartz RD, Crofford LJ, Phan SH, Ike RW, Su LD: Nephrogenic fibrosing dermopathy: A novel cutaneous fibrosing disorder in patients with renal failure. Am J Med. 114:: p. 563 –572, 2003. [PubMed]

5. Levine JM, Taylor RA, Elman LB, Bird SJ, Lavi E, Stolzenberg ED, McGarvey ML, Asbury AK, Jimenez SA: Involvement of skeletal muscle in dialysis-associated systemic fibrosis (nephrogenic fibrosing dermopathy). Muscle Nerve. 30:: p. 569 –577, 2004. [PubMed]

6. Hauser C, Kaya G, Chizzolini C: Nephrogenic fibrosing dermopathy in a renal transplant recipient with tubulointerstitial nephritis and uveitis. Dermatology. 209:: p. 50 –52, 2004. [PubMed]

7. Gambichler T, Paech V, Kreuter A, Wilmert M, Altmeyer P, Stucker M: Nephrogenic fibrosing dermopathy. Clin Exp Dermatol. 29:: p. 258 –260, 2004. [PubMed]

8. Gibson SE, Farver CF, Prayson RA: Multiorgan involvement in nephrogenic fibrosing dermopathy: An autopsy case and review of the literature. Arch Pathol Lab Med. 130:: p. 209 –212, 2006. [PubMed]

9. Najafian B, Franklin DB, Fogo AB: Acute renal failure and myalgia in a transplant patient. J Am Soc Nephrol. 18:: p. 2870 – 2874, 2007. [PubMed]

10. Mendoza FA, Artlett CM, Sandorfi N, Latinis K, Piera-Velazquez S, Jimenez SA: Description of 12 cases of nephrogenic fibrosing dermopathy and review of the literature. Semin Arthritis Rheum. 35:: p. 238 –249, 2006. [PubMed]

11. Othersen JB, Maize JC, Woolson RF, Budisavljevic MN: Nephrogenic systemic fibrosis after exposure to gadolinium in patients with renal failure. Nephrol Dial Transplant. 22:: p. 3179 –3185, 2007. [PubMed]

12. Nephrogenic fibrosing dermopathy associated with exposure to gadolinium-containing contrast agents—St. Louis, Missouri, 2002–2006. MMWR Morb Mortal Wkly Rep. 56:: p. 137 –141, 2007. [PubMed]

13. Plamondon I, Samson C, Watters AK, Begin LR, Cote J, Deziel C, Querin S: Nephrogenic systemic fibrosis: More hard times for renal failure patients [in French]. Nephrol Ther. 3:: p. 152 –156, 2007. [PubMed]

14. Swaminathan S, Shah SV: New insights into nephrogenic systemic fibrosis. J Am Soc Nephrol. 18:: p. 2636 –2643, 2007. [PubMed]

15. Todd DJ, Kagan A, Chibnik LB, Kay J: Cutaneous changes of nephrogenic systemic fibrosis: Predictor of early mortality and association with gadolinium exposure. Arthritis Rheum. 56:: p. 3433 –3441, 2007. [PubMed]

16. Lim YL, Lee HY, Low SC, Chan LP, Goh NS, Pang SM: Possible role of gadolinium in nephrogenic systemic fibrosis: Report of two cases and review of the literature. Clin Exp Dermatol. 32:: p. 353 –358, 2007. [PubMed]

17. Galan A, Cowper SE, Bucala R: Nephrogenic systemic fibrosis (nephrogenic fibrosing dermopathy). Curr Opin Rheumatol. 18:: p. 614 –617, 2006. [PubMed]

18. Boyd AS, Zic JA, Abraham JL: Gadolinium deposition in nephrogenic fibrosing dermopathy. J Am Acad Dermatol. 56:: p. 27 –30, 2007. [PubMed]

19. Cowper SE, Bucala R, Leboit PE: Nephrogenic fibrosing dermopathy/nephrogenic systemic fibrosis: Setting the record straight. Semin Arthritis Rheum. 35:: p. 208 –210, 2006. [PubMed]

20. Grobner T: Gadolinium: A specific trigger for the development of nephrogenic fibrosing dermopathy and nephrogenic systemic fibrosis? Nephrol Dial Transplant. 21:: p. 1104 –1108, 2006. [PubMed]

21. Marckmann P, Skov L, Rossen K, Dupont A, Damholt MB, Heaf JG, Thomsen HS: Nephrogenic systemic fibrosis: Suspected causative role of gadodiamide used for contrast-enhanced magnetic resonance imaging. J Am Soc Nephrol. 17:: p. 2359 –2362, 2006. [PubMed]

22. Grobner T, Prischl FC: Gadolinium and nephrogenic systemic fibrosis. Kidney Int. 72:: p. 260 –264, 2007. [PubMed]

23. Heinrich M, Uder M: Nephrogenic systemic fibrosis after application of gadolinium-based contrast agents: A status paper [in German]. Rofo. 179:: p. 613 –617, 2007. [PubMed]

24. Peak AS, Sheller A: Risk factors for developing gadolinium-induced nephrogenic systemic fibrosis. Ann Pharmacother. 41:: p. 1481 –1485, 2007. [PubMed]

25. Idee JM, Port M, Raynal I, Schaefer M, Le Greneur S, Corot C: Clinical and biological consequences of transmetallation induced by contrast agents for magnetic resonance imaging: A review. Fundam Clin Pharmacol. 20:: p. 563 –576, 2006. [PubMed]

26. Tweedle MF, Hagan JJ, Kumar K, Mantha S, Chang CA: Reaction of gadolinium chelates with endogenously available ions. Magn Reson Imaging. 9:: p. 409 –415, 1991. [PubMed]

27. Cacheris WP, Quay SC, Rocklage SM: The relationship between thermodynamics and the toxicity of gadolinium complexes. Magn Reson Imaging. 8:: p. 467 –481, 1990. [PubMed]

28. Franano FN, Edwards WB, Welch MJ, Brechbiel MW, Gansow OA, Duncan JR: Biodistribution and metabolism of targeted and nontargeted protein-chelate-gadolinium complexes: Evidence for gadolinium dissociation in vitro and in vivo. Magn Reson Imaging. 13:: p. 201 –214, 1995. [PubMed]

29. Rehwald WG, Fieno DS, Chen EL, Kim RJ, Judd RM: Myocardial magnetic resonance imaging contrast agent concentrations after reversible and irreversible ischemic injury. Circulation. 105:: p. 224 –229, 2002. [PubMed]

30. Mizgerd JP, Molina RM, Stearns RC, Brain JD, Warner AE: Gadolinium induces macrophage apoptosis. J Leukoc Biol. 59:: p. 189 –195, 1996. [PubMed]

31. Thakral C, Alhariri J, Abraham JL: Long-term retention of gadolinium in tissues from nephrogenic systemic fibrosis patient after multiple gadolinium-enhanced MRI scans: Case report and implications. Contrast Media Mol Imaging. 2:: p. 199 –205, 2007. [PubMed]

32. Thakral C, Abraham JL: Automated scanning electron microscopy and x-ray microanalysis for in situ quantification of Gadolinium deposits in skin. J Electron Microsc (Tokyo). 156:: p. 181 –187, 2007

33. High WA, Ayers RA, Chandler J, Zito G, Cowper SE: Gadolinium is detectable within the tissue of patients with nephrogenic

systemic fibrosis. J Am Acad Dermatol. 56:: p. 21 –26, 2007. [PubMed]

34. High WA, Ayers RA, Cowper SE: Gadolinium is quantifiable within the tissue of patients with nephrogenic systemic fibrosis. J Am Acad Dermatol. 56:: p. 710 –712, 2007. [PubMed]

35. Reimer L, Deininger C, Egerton RF, Hofer F, Jouffrey B, Krahl D, Leapman RD, Mayer J, Rose H, Schattschneider P, Spence JC: Electron-Filtering Transmission Electron Microscopy. , Berlin, Springer, 1995

36. Leapman RD, Sun SQ, Hunt JA, Andrews SB: Biological electron energy loss spectroscopy in the field-emission scanning transmission electron microscope. Scanning Microsc Suppl. 8:: p. 245 –258, discussion 258–259, 1994. [PubMed]

37. Egerton RF: Electron Energy-Loss Spectroscopy in the Electron Microscope. , New York, Plenum Press, 1986

38. Simon GT, Heng YM: Electron energy loss spectroscopic imaging in biology. Scanning Microsc. 2:: p. 257 –266, 1988. [PubMed]

39. Egerton RF: New techniques in electron energy-loss spectroscopy and energy-filtered imaging. Micron. 34:: p. 127 –139, 2003. [PubMed]

40. Egerton RF: Limits to the spatial, energy and momentum resolution of electron energy-loss spectroscopy. Ultramicroscopy. 107:: p. 575 –586, 2007. [PubMed]

41. Keast VJ, Bosman M: New developments in electron energy loss spectroscopy. Microsc Res Tech. 70:: p. 211 –219, 2007. [PubMed]

42. Kapp N, Studer D, Gehr P, Geiser M: Electron energy-loss spectroscopy as a tool for elemental analysis in biological specimens. In: Electron Microscopy, Methods and Protocols. , 2nd Ed., edited by John K, Totowa, NJ, Humana Press, 2007. , pp p. 431 –447

43. Kapp N, Kreyling W, Schulz H, Im Hof V, Gehr P, Semmler M, Geiser M: Electron energy loss spectroscopy for analysis of inhaled ultrafine particles in rat lungs. Microsc Res Tech. 63:: p. 298 –305, 2004. [PubMed]

44. Rothen-Rutishauser BM, Schurch S, Haenni B, Kapp N, Gehr P: Interaction of fine particles and nanoparticles with red blood cells visualized with advanced microscopic techniques. Environ Sci Technol. 40:: p. 4353 –4359, 2006. [PubMed]

45. Geiser M, Rothen-Rutishauser B, Kapp N, Schurch S, Kreyling W, Schulz H, Semmler M, Im Hof V, Heyder J, Gehr P: Ultrafine particles cross cellular membranes by nonphagocytic mechanisms in lungs and in cultured cells. Environ Health Perspect. 113:: p. 1555 –1560, 2005. [PubMed]

46. Hirai K, Pan J, Shimada H, Izuhara T, Kurihara T, Moriguchi K: Cytochemical energy-filtering transmission electron microscopy of mitochondrial free radical formation in paraquat cytotoxicity. J Electron Microsc (Tokyo). 48:: p. 289 –296, 1999. [PubMed]

47. Rouelle-Rossier VB, Biggiogera M, Fakan S: Ultrastructural detection of calcium and magnesium in the chromatoid body of mouse spermatids by electron spectroscopic imaging and electron energy loss spectroscopy. J Histochem Cytochem. 41:: p. 1155 –1162, 1993. [PubMed]

48. Schlotzer-Schrehardt U, Kortje KH, Erb C: Energy-filtering transmission electron microscopy (EFTEM) in the elemental analysis of pseudoexfoliative material. Curr Eye Res. 22:: p. 154 –162, 2001. [PubMed]

49. Jonas L, Baguhl F, Wilken HP, Haas HJ, Nizze H: Copper accumulation in actinomyces druses during endometritis after long-term use of an intrauterine contraceptive device. Ultrastruct Pathol. 26:: p. 323 –329, 2002. [PubMed]

50. Jonas L, Fulda G, Kroning G, Merkord J, Nizze H: Electron microscopic detection of tin accumulation in biliopancreatic concrements after induction of chronic pancreatitis in rats by di-n-butyltin dichloride. Ultrastruct Pathol. 26:: p. 89 –98, 2002. [PubMed]

51. Schroeder JA, Voelkl E, Hofstaedter F: Ultrastructural telepathology: Remote EM-diagnostic via Internet. Ultrastruct Pathol. 25:: p. 301 –307, 2001. [PubMed]

52. Reimer L, Zedke U, Moesch J, Schulze-Hillert ST, Ross-Messemer M, Probst W, Weimer E: EELS-Spectroscopy: A Reference

Handbook of Standard Data for the Identification and Interpretation of Electron Energy Loss Spectra and for Generation of Electron Spectra Images. , Oberkochen, Carl Zeiss Electron Optic Division, 1992

53. Wahba IM, Simpson EL, White K: Gadolinium is not the only trigger for nephrogenic systemic fibrosis: Insights from two cases and review of the recent literature. Am J Transplant. 7:: p. 2425 –2432, 2007. [PubMed]

54. Eyden B: The Myofibroblast: A Study of Normal, Reactive and Neoplastic Tissues with an Emphasis on Ultrastructure. , Siena, Nuova Immagine Editrice, 2007

55. Quan TE, Cowper S, Wu SP, Bockenstedt LK, Bucala R: Circulating fibrocytes: Collagen-secreting cells of the peripheral blood. Int J Biochem Cell Biol. 36:: p. 598 –606, 2004. [PubMed]

56. Schmidt M, Sun G, Stacey MA, Mori L, Mattoli S: Identification of circulating fibrocytes as precursors of bronchial myofibroblasts in asthma. J Immunol. 171:: p. 380 –389, 2003. [PubMed]

57. Cowper SE, Kuo PH, Bucala R: Nephrogenic systemic fibrosis and gadolinium exposure: Association and lessons for idiopathic fibrosing disorders. Arthritis Rheum. 56:: p. 3173 –3175, 2007. [PubMed]

58. Stöger M: ELNES—Energy Loss Near Edge Structure, 2002. Available at: http://tem.atp.tuwien.ac.at/EELS/ELNES.htm. Accessed November 19, 2007

59. Jouffrey B, Schattschneider P, Hebert C: Ionization edges: Some underlying physics and their use in electron microscopy. In: Advances in Imaging and Electron Physics. , edited by Hawkes PW, San Diego, Academic Press, Elsevier Science, 2002. , pp p. 413 –450
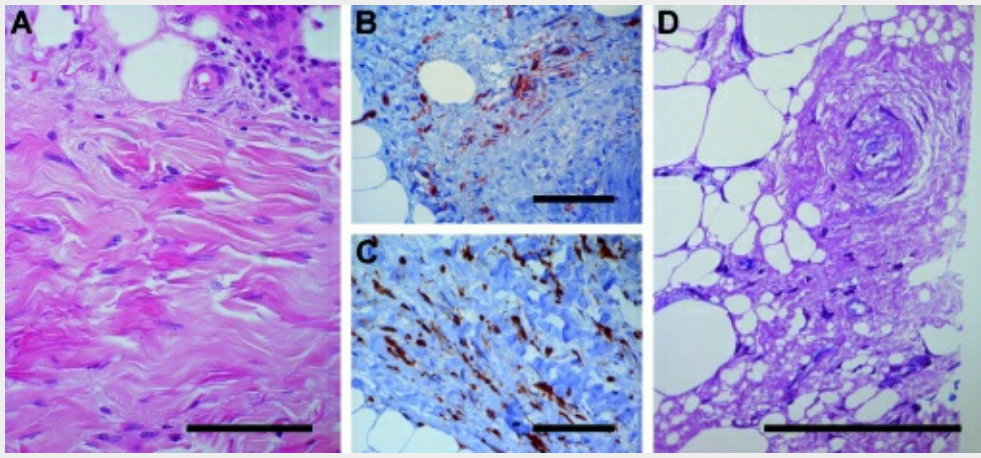
Figure 1.

Deep skin biopsy. (A) Hematoxylin and eosin stain showing dense dermal fibrosis with spindle cells and slight perivascular cellular infiltrate. (B) CD34^{+} spindle cells between collagen bands. (C) Area with numerous CD68^{+} histiocytic cells. (D) Double toluidine blue/fuchsin-stained semithin resin section showing a fragment of the wax-reprocessed tissue containing a blood vessel selected for EM study. Bar = 100 µm.
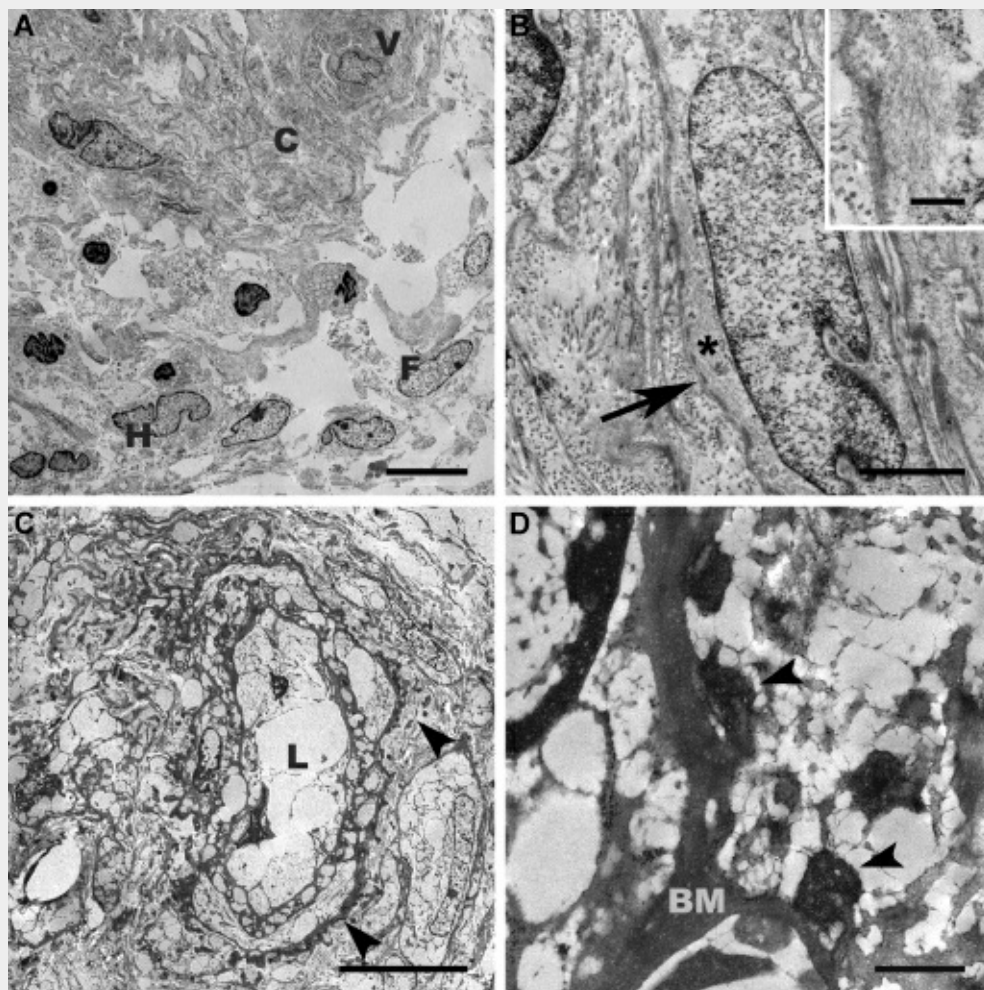
Figure 2.

Conventional EM of deparaffinized skin tissue. (A) Low-magnification overview of the dermis displaying bundles of collagen (C) with clefts, profile of a small blood vessel (V), histiocytes (H), fibroblastic (F), and inflammatory cells. Bar = 10 μm. (B) Closer view at a higher differentiated elongated cell presenting myofibroblastic hallmarks including attachment plaques (arrow) and bundles of intermediate filaments (* and insert). Bar = 2 μm (insert bar = 500 nm). (C) Overview showing a blood vessel with empty lumen (L) and numerous tiny deposits (arrowheads) at the external side of the basal lamina. Bar = 10 μm. (D) Features noted at higher magnification of the irregular-shaped deposits with fine-granular texture mostly adhering to the basal membrane (BM). Bar = 500 nm. (C and D) Images captured during telepathologic second-opinion retrieval.
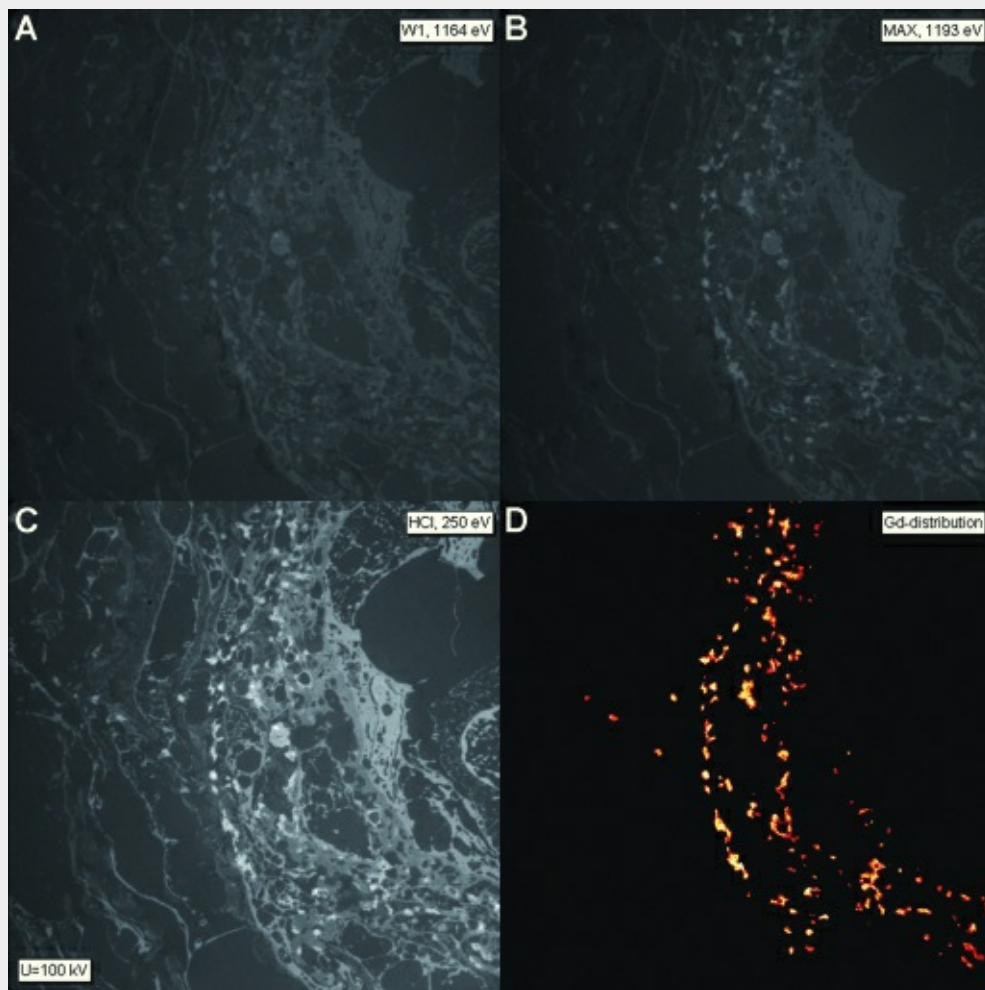
Figure 3.

ESI: Overview of images taken from an unstained skin section showing the perivascular region of a blood vessel using inelastic scattered electrons. (A) Background image at 1164 eV energy loss. (B) Image taken at the maximum of the Gd-specific signal at 1193 eV energy loss. (C) Structure-sensitive image (HCI) taken at 250 eV energy loss before the carbon-specific signal; note the dark field–like structure visualization. (D) Net Gd signal calculated by subtracting the extrapolated background image from the Gd-specific signal. The obtained image reflects the Gd distribution and is displayed in red color; yellow color is attributed to more intense element signal. Magnification, ×2100.
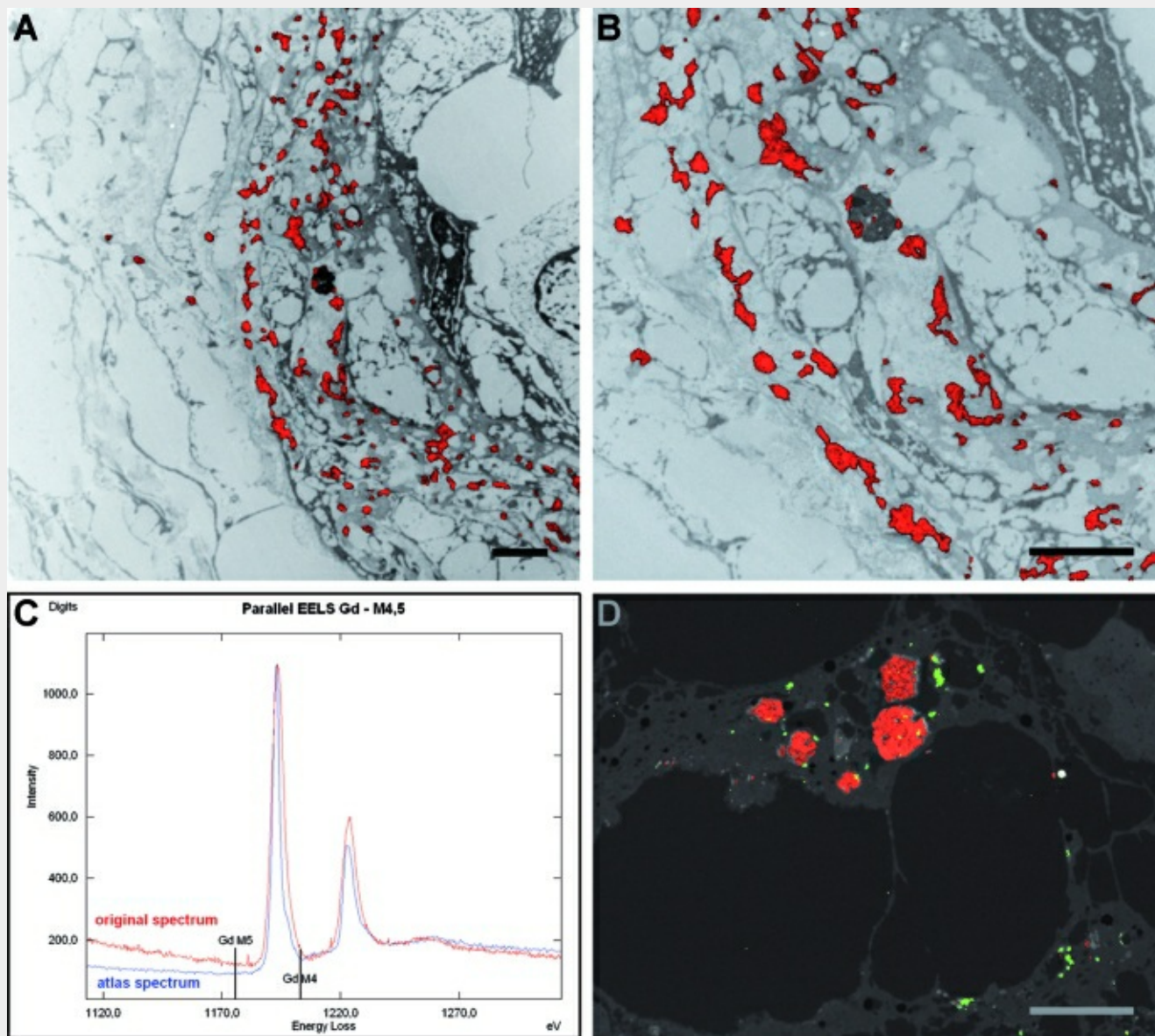
Figure 4.

ESI and parallel EELS. (A) Gd mapping in the skin lesion at low magnification. The net Gd signal image is superimposed on the inverted HCI image showing the precise localization of the signals as red spots on the tissue structures. Note the dispersed Gd aggregates in the perivascular zone of the blood vessel and only singular deposits in the adjacent tissue. (B) Higher magnification of portion of A showing detailed features of the Gd deposits and their multifocal association with the blood vessel basal lamina, cell profiles, and collagen fibrils. In the dark lysosomal structure, Gd signal is visible only at the periphery. (C) Parallel EELS spectrum. The confirmation of a particular element is demonstrated by its defined energy-loss edge at the energy level necessary for atom inner shell ionization. Record of the measured (spot mode) Gd signal (red) displaying the typical "white line" peaks characteristic for Gd. For comparison, the reference Gd spectrum from the element atlas (blue). (D) Simultaneous Gd and iron mapping in deep dermis. Both net Gd (red) and iron (green) signal were combined with the original HCI image. Note the iron signal co-localization in the Gd deposits (orange dots) and their periphery as well as small iron aggregates in the adjacent tissue. Bar = 2 µm (all images).